JCTC Journal of Chemical Theory and Computation

pubs.acs.org/JCTC Article

Modified Activation-Relaxation Technique (ARTn) Method Tuned for Efficient Identification of Transition States in Surface Reactions

Jisu Jung, Hyungmin An, Jinhee Lee, and Seungwu Han*

Cite This: J. Chem. Theory Comput. 2024, 20, 8024−8034 Read Online

ACCESS | Metrics & More | Article Recommendations | Supporting Information

ABSTRACT: Exploring potential energy surfaces (PES) is essential for unraveling the underlying mechanisms of chemical reactions and material properties. While the activation-relaxation technique (ARTn) is a state-of-the-art method for identifying saddle points on PES, it often faces challenges in complex energy landscapes, especially on surfaces. In this study, we introduce iso-ARTn, an enhanced ARTn method that incorporates constraints on an orthogonal hyperplane and employs an adaptive active volume. By leveraging a neural network potential (NNP) to conduct an exhaustive saddle point search on the Pt(111) surface with 0.3 monolayers of surface oxygen coverage, iso-ARTn achieves a success rate that is 8.2% higher than the original ARTn, with 40% fewer force calls. Moreover, this method effectively finds various saddle points without compromising the success rate. Combined with kinetic Monte Carlo simulations for event table construction, iso-ARTn with NNP demonstrates the capability to reveal structures consistent with experimental observations. This work signifies a substantial advancement in the investigation of PES, enhancing both the efficiency and breadth of saddle point searches.

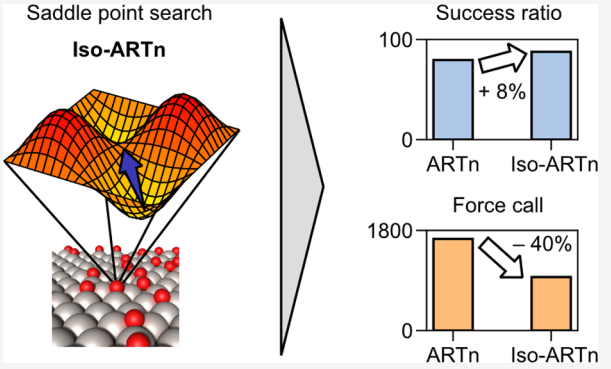

1. INTRODUCTION

Chemical processes at surfaces, such as catalysis, corrosion, and thin-film growth, lie at the heart of materials science and engineering. They consist of diverse surface reactions such as adsorption, dissociation, association, diffusion, and desorption.[1−3] In explaining and predicting the outcomes of processes theoretically, a mechanistic model is indispensable, which lays out the sequence of reactions and intermediates as reactants are transformed into products. Building such a model, in turn, requires computational machinery that can identify possible surface reactions or intermediates from the given surface state. The most straightforward approach would be to follow the process through molecular dynamics (MD) simulations, which produce atomic trajectories according to Newton's laws of motion under the given Hamiltonian. However, many chemical reactions occur over time scales far longer than nanoseconds, which are the maximum time span for typical MD simulations; thus, MD has inherent limitations in directly observing chemical reactions.[4] In bulk systems, one can accelerate the dynamics by increasing the temperature,[5] but this approach can overly promote evaporation in surface simulations due to entropic effects.

Another, more widely practiced approach is to identify elementary surface reactions individually, which consist of the initial state (IS), transition state (TS), and final state (FS), to understand the surface process as a Markovian reaction chain.[6] Here, two distinct methods exist depending on how the reaction pathway is explored. The "FS-first" method attempts to locate subsequent surface states or intermediates first that can be reached from the given IS through a one-step reaction. In many cases, plausible states are selected by human intuition,[7,8] but graph-based methods[9−11] and stochastic potential energy surface (PES) walker[12] have been also developed for systematic and automated identification. Once the FS is known, double-ended approaches such as nudged elastic-band method[13] and string method[14,15] efficiently find the minimum energy pathway including the TS. However, the FS-first methods have been mostly applied to molecular reactions on the surface where possible bond pairs are limited and can be reasonably guessed by established chemistry. For more complicated processes such as surface oxidation where atoms are collectively bonded and multiple reaction pathways exist,[16,17] the FS-first approach can miss unexpected products or pathways.

On the other hand, in the "TS-first" method, the TS connected to the given IS is searched for first by driving the PES explorer from the harmonic basin toward a first-order saddle point that has only one negative eigenvalue in the

Received: June 13, 2024
Revised: August 23, 2024
Accepted: August 30, 2024
Published: September 6, 2024

https://doi.org/10.1021/acs.jctc.4c00767
J. Chem. Theory Comput. 2024, 20, 8024−8034

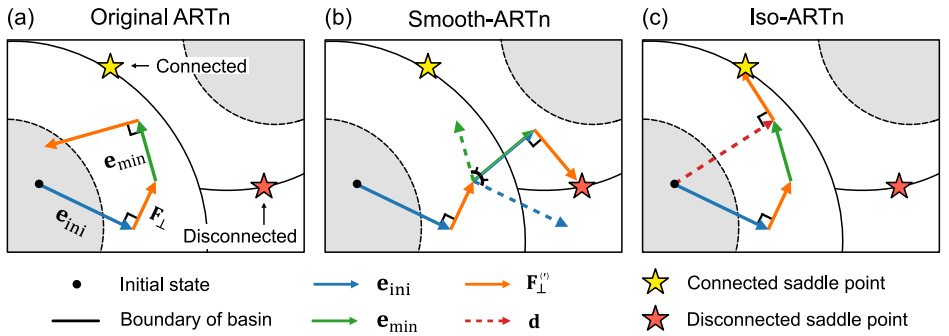

Figure 1. Schematic comparison of various ARTn methods. In (a−c), solid lines represent the original, smooth-, and iso-ARTn trajectories, respectively, while dashed lines serve as guidelines. The shaded area means that λ is positive.

Hessian matrix. Once the TS is identified, the FS can be obtained by relaxing the TS along the negative eigenmode, away from the IS, provided that post-TS bifurcations are absent.[18] The TS-first method has been successfully applied to various surface reactions, including atomic layer deposition of TiN on Cu(111) and Si(100),[19,20] the decomposition of HCOO and CH_3OH on the Cu(111) and (110),[21,22] adatom diffusion on Al and Fe surfaces,[23,24] and vacancy diffusion on anatase (101) surface.[25] Among the various TS-first approaches,[26−29] minimum-mode following methods such as the dimer method[23] and activation-relaxation technique nouveau (ARTn)[30−32] have been tailored to identify TS in complex and high-dimensional systems such as condensed phases with manageable computational costs.[33] The dimer method adjusts two images to align with the minimum eigenmode of the Hessian matrix, while ARTn employs the Lanczos algorithm.[34] Without presuming the nature of the products, the dimer method and ARTn are also efficient for generating a fully connected PES with multiple saddle points. This is particularly useful for on-the-fly kinetic Monte Carlo (kMC) methods, in which the event table is updated after each kMC step.[35,36] However, heavy computational loads in locating the TS limit the application system when the PES is evaluated by ab initio methods such as density functional theory (DFT).

On the surface, the under-coordinated atoms can move more freely than in the bulk system, where atomic positions are strongly restricted by surrounding atoms within deep harmonic basins. This generates many soft modes and makes the PES complex with numerous shallow basins. Such PES characteristic poses significant challenges to the TS-searching algorithm. For instance, while searching for saddle points from the minimum state, the algorithm is prone to falling into adjacent irrelevant basins, resulting in the identification of disconnected saddle points. As will be shown in this study, we find that the state-of-the-art TS-searching methods are less efficient in dealing with surface reactions with complex PES compared to typical bulk systems, which motivates us to develop a modified ARTn tailored for surface reactions. Additionally, we aim to develop a TS-searching method capable of identifying elementary reactions across the entire surface, rather than focusing solely on isolated reactions around specific sites. We achieve this goal by introducing two improvements: First, we suggest a new algorithm dubbed iso-ARTn, which effectively prevents the PES explorer from drifting to disconnected saddle points or returning to the IS. Second, we introduce an adaptive active volume that progressively expands its size, a feature necessary when reactions are densely distributed across a large area.

We showcase the efficiency of our scheme with a 1.9 × 2.2 nm^2 Pt(111) surface with 0.3 monolayers of surface O coverage, a configuration appearing in the initial oxidation stage of the Pt surface. During this oxidation process, adsorbed O atoms diffuse across the surface and penetrate the subsurface, while Pt atoms are displaced from their lattice positions through a Pt-buckling mechanism.[17] This displacement leads to the formation of a planar Pt−O structure and creates space for further oxygen penetration.[37] These steps may result in significant surface reconstruction, leading to a phase transition from Pt to PtO_2. This complex oxidation mechanism serves as an ideal test case for evaluating the performance of iso-ARTn. It is also crucial for the durability of electrocatalysts in fuel cells[38] and for the reactivity of heterocatalysts in CO oxidation.[39] To accelerate the computation, we employ a Behler−Parrinello neural network potential (NNP)[40] that is trained on DFT reference data.

The rest of the paper is organized as follows: Section 2 introduces the ARTn and its variations, including iso-ARTn, and explains the adaptive active volume. In Section 3, we discuss the results of this work, including the validation of the trained NNP and the performance evaluation of iso-ARTn. Finally, Section 4 concludes the paper.

2. THEORY AND ALGORITHM

2.1. Original ARTn. In this subsection, we briefly overview the original framework of ARTn and one recent algorithmic improvement. Initially, the system lies at a local minimum with the collective coordinate $\mathbf{r}$ equal to $\mathbf{r}_0$. The initial push direction ($\hat{\mathbf{e}}_{ini}$) is provided by the user or generated randomly. By varying $\hat{\mathbf{e}}_{ini}$, one can obtain diverse saddle points connected to the IS. To reach the first-order saddle points where only one eigenvalue is negative, ARTn undergoes a series of activation and orthogonal relaxation (see Figure 1). First, the minimum eigenvalue (λ) of the Hessian matrix is calculated together with its corresponding eigenvector ($\hat{\mathbf{e}}_{min}$) using the Lanczos method,[34] which allows for obtaining $\hat{\mathbf{e}}_{min}$ without evaluating the full Hessian matrix. By convention, $\hat{\mathbf{e}}_{min}$ is directed toward higher energy. In the activation step, the system is pushed along the direction ($\hat{\mathbf{e}}$) defined as follows

$$\hat{\mathbf{e}} = \begin{cases} \hat{\mathbf{e}}_{ini} & \text{if } \lambda > 0 \\ \hat{\mathbf{e}}_{min} & \text{if } \lambda \leq 0 \end{cases} \quad (1)$$

That is to say, the system is pushed along $\hat{\mathbf{e}}_{ini}$ within the harmonic basin while it follows $\hat{\mathbf{e}}_{min}$ outside the basin. For

https://doi.org/10.1021/acs.jctc.4c00767
J. Chem. Theory Comput. 2024, 20, 8024−8034

rapid convergence to TS, the step size during the activation (Δr) is adaptively set[41]

$$\Delta r = \begin{cases} \Delta r_{\max} & \text{if } \lambda > 0 \\ \min\left(\Delta r_{\max}, \dfrac{|\mathbf{F}_{\parallel}|}{|\lambda|}\right) & \text{if } \lambda \le 0 \end{cases} \tag{2}$$

where $\Delta r_{\max}$ is a user-defined maximum step size, and $\mathbf{F}_{\parallel}$ is the component of collective atomic force vector ($\mathbf{F}$) parallel to $\hat{\mathbf{e}}$, i.e., $\mathbf{F}_{\parallel} = (\mathbf{F}\cdot\hat{\mathbf{e}})\hat{\mathbf{e}}$. Thus, the system moves from the current position $\mathbf{r}$ to $\mathbf{r} + \Delta r\hat{\mathbf{e}}$.

After each activation step, the system is relaxed in energy within the hyperplane orthogonal to $\hat{\mathbf{e}}$, resulting in a downward shift in the PES. Within the harmonic basin, the relaxation step helps find TS with low activation energies whereas it enables the PES explorer to approach TS outside the basin. During relaxation, the conjugate gradient (CG) method can be employed utilizing orthogonal atomic forces ($\mathbf{F}_{\perp} = \mathbf{F} - \mathbf{F}_{\parallel}$) to $\hat{\mathbf{e}}$.[42,43] The number of CG steps varies depending on the sign of λ: the system undergoes a fixed number of CG steps when $\lambda > 0$, but for $\lambda < 0$, the relaxation continues until $|\mathbf{F}_{\perp}| < |\mathbf{F}_{\parallel}|$. The activation-relaxation procedure is repeated until $\lambda < 0$ and $|\mathbf{F}|$ is smaller than a predefined tolerance (ϵ), which signifies that the system arrives at the first-order saddle point.

The original ARTn modifies $\hat{\mathbf{e}}$ discontinuously as λ changes sign (see eq 1). Such abrupt transition can inadvertently direct the system back into the harmonic basin during the ensuing relaxation step, requiring further iterations to reach connected saddle points or even leading to convergence to irrelevant ones. In ref 32, this problem was addressed by introducing a mixing function that gradually alters $\hat{\mathbf{e}}$ from $\hat{\mathbf{e}}_{\text{ini}}$ to $\hat{\mathbf{e}}_{\min}$ in the activation step (called smooth-ARTn in this study) when λ becomes negative

$$\hat{\mathbf{e}} = (1-\eta)\hat{\mathbf{e}}_{\text{ini}} + \eta\hat{\mathbf{e}}_{\min} \tag{3}$$

where η denotes the mixing coefficient which increases from 0 to 1 over a certain number of iterations. For the interstitial defects in the Si bulk crystal, the smooth-ARTn increased the success rate from 33 to 87%.[32]

The smooth-ARTn approach postpones alignment with $\hat{\mathbf{e}}_{\min}$ for a few steps after the system escapes from the harmonic basin. However, in the presence of many shallow basins, as in surface reactions, such a gradual change in $\hat{\mathbf{e}}$ can easily lead the system to traverse the boundary of the initial basin, converging to disconnected saddle points.

2.2. Iso-ARTn. In the above, we pointed out weaknesses in original and smooth-ARTn. To address these, we introduce a new variant of ARTn referred to as iso-ARTn. The iso-ARTn follows the original ARTn except for the hyperplane on which the system is relaxed. In the original scheme, the hyperplane is orthogonal only to $\hat{\mathbf{e}}$. In the iso-ARTn, the hyperplane is additionally conditioned to be orthogonal to the displacement vector $\mathbf{d}$ from the IS to the current position ($\mathbf{d} = \mathbf{r} - \mathbf{r}_0$). This constraint in relaxation is easily imposed by adjusting the orthogonal atomic forces used in CG as follows

$$\mathbf{F}'_{\perp} = \mathbf{F}_{\perp} - (\mathbf{F}\cdot\hat{\mathbf{d}}_{\perp})\hat{\mathbf{d}}_{\perp} = \mathbf{F} - (\mathbf{F}\cdot\hat{\mathbf{e}})\hat{\mathbf{e}} - (\mathbf{F}\cdot\hat{\mathbf{d}}_{\perp})\hat{\mathbf{d}}_{\perp} \tag{4}$$

where $\mathbf{d}_{\perp} = \mathbf{d} - (\mathbf{d}\cdot\hat{\mathbf{e}})\hat{\mathbf{e}}$. Eq 4 also defines $\mathbf{F}'_{\parallel} = \mathbf{F} - \mathbf{F}'_{\perp}$. Since the system is relaxed while being orthogonal to $\mathbf{d}$ ($\mathbf{F}'_{\perp}\cdot\mathbf{d} = 0$), the Euclidean distance from the original position $\mathbf{r}_0$ is preserved in the limit of small relaxation step size. This prevents the PES explorer from relaxing back to the IS, which is the drawback of the original ARTn. On the other hand, $\hat{\mathbf{e}}$ instantly changes from $\hat{\mathbf{e}}_{\text{ini}}$ to $\hat{\mathbf{e}}_{\min}$ as soon as the system escapes from the basin, which prevents the system from drifting to disconnected saddle point. The additional orthogonal condition to the displacement vector is lifted near saddle points.

Figure 1 illustrates a schematic comparison of original ARTn, smooth-ARTn, and iso-ARTn. In Figure 1a, the original ARTn may return to the initial harmonic basin (the shaded areas) due to a sudden change in $\hat{\mathbf{e}}$ (as depicted by the arrows changing from blue to green), which requires the system to climb out of the harmonic basin again. Smooth-ARTn in Figure 1b changes $\hat{\mathbf{e}}$ progressively, which can lead to crossing the boundary of the initial basin and, consequently, to disconnected saddle points. Iso-ARTn in Figure 1c prevents the system from either returning to the harmonic basin or crossing the boundary by maintaining the distance from the IS.

2.3. Adaptive Active Volume. Because chemical reactions occur within localized areas, the dimensions of the search space can be reduced by introducing an active volume.[44] Within this volume, atoms are permitted to move during the search for the saddle point, while atoms outside this volume remain fixed. Employing the active volume can significantly reduce the computational cost by either skipping force calculations for fixed atoms or excluding the atoms that are far from the active volume entirely, where the influence of displaced atoms is negligible. Furthermore, the reduction in degrees of freedom leads to a smaller Hessian matrix, which accelerates the convergence to saddle points in the more focused search space. This is particularly useful when the model dimensions are much larger than the typical reaction radius ($\lesssim 6$ Å). The radius of the active volume should be large enough so that the effect of the reaction is negligible outside the boundary of the active volume. It can also be dynamically reduced during the saddle point search since typically only a small group of atoms are displaced at the saddle points.[45]

In most previous applications employing the active volume, it was sufficient to define a fixed active volume specifically centered around defects or adsorbates where atoms are likely to move because these sites were typically isolated due to their low density, making it easier to focus the active volume on a single and well-defined region. However, in surface oxidation, as demonstrated in the present study, the reaction centers are more densely distributed across the surface due to the adsorption of many oxygen atoms, meaning that reactions can occur not just at the center of the active volume but also near its boundaries. To consider this, we suggest an adaptive active volume in which the active volume expands by tracing the reaction center. It first starts with an initial active volume (V_0) that is a sphere centered on a specific atom. After a few steps of ARTn, the i-th atom with the maximum displacement from $\mathbf{r}_0$ is identified, and the active volume is iteratively updated as follows

$$V_{k+1} = V_k \cup S_i \qquad (k = 0, 1, 2, \ldots) \tag{5}$$

where S_i is the sphere with a certain radius centered at the i-th atom. The radius of S_i can be adjusted, provided that the energy of the saddle point converges within acceptable limits,[44] as interactions with atoms outside active volume are still considered in force calculation. The adaptive active volume updates its size by including the new active volume centered on the atom that has undergone the maximum displacement

https://doi.org/10.1021/acs.jctc.4c00767
J. Chem. Theory Comput. 2024, 20, 8024−8034

from the IS. Once the system converges to a saddle point within the given adaptive volume, the TS search proceeds using the full-dimensional PES to guarantee the fidelity of the saddle point. Since the adaptive active volume increases the number of moving atoms, the computational cost inevitably increases. However, the final number of atoms is usually 2−3 times the original number, and the increase in the computational time is moderate.

Figure 2 shows the basic flowchart of the current method combining iso-ARTn and adaptive active volume.

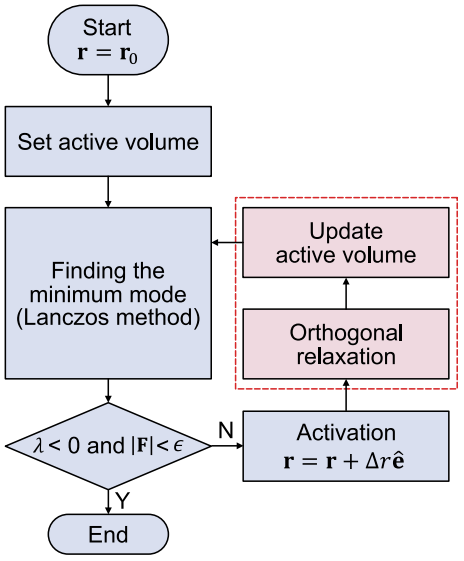

Figure 2. Flowchart of the ARTn used in this work. $\mathbf{r}$ and $\mathbf{r}_0$ denote the position vector and the initial position vector, respectively. λ stands for the minimum eigenvalue of the Hessian matrix. $\mathbf{F}$ represents the atomic force vector, and ϵ is the threshold for force convergence. Δr and $\hat{\mathbf{e}}$ correspond to the step size and unit vector along the push direction, respectively. The iso-ARTn and adaptive active volume developed in the present work are shown in the dashed box.

2.4. Computational Package. We have developed the SHERPA (Saddle points Hunting based on Energy surface for Reaction PAthways) package, which implements previously discussed algorithms (original, smooth-, and iso-ARTn, and adaptive active volume). The package also features the dimer method and its variant.[23,46] SHERPA directly interfaces with two simulation tools, VASP[47,48] and LAMMPS,[49] to obtain the energies and forces from configurations. Additionally, SHERPA can interact with other simulators through the Python-based ASE package,[50] providing a flexible interface for various simulation platforms.

3. RESULTS AND DISCUSSION

In this section, to compare various ARTn methods in a practical application, we consider a 5-layer 8 × 8 Pt(111) slab covered with 0.3 monolayers of O adatoms (Figure 3). This represents the initial stage of the platinum oxidation process, where the O atoms cover the Pt surface up to half monolayers under a voltage range of 0.85−1.15 V with respect to the reference hydrogen electrode.[51] Using ARTn, we identify saddle points from the given structure and compare the outcomes. To enable diverse surface reactions, the O atoms are randomly distributed on both FCC and HCP sites, although

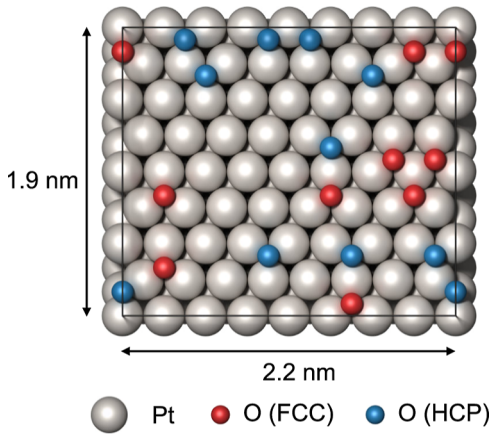

Figure 3. Top view of the model system for testing various ARTn methods. The silver atoms stand for the Pt atom, while the red and blue atoms represent O atoms at FCC and HCP sites, respectively.

FCC sites are more stable than HCP sites by 0.43 eV. For an extensive test, we employ the NNP in Section 3.1. The computational results are compared in Section 3.2 with further analysis in Section 3.3. In Section 3.4, we investigate whether all the low-lying saddle points are detected by iso-ARTn. In Section 3.5, we conduct an on-the-fly kMC simulation on Pt-oxidation process using iso-ARTn.

3.1. Neural Network Potential. To train NNP for simulating Pt−O system in Figure 3, we prepare the DFT training set designed to cover diverse local motifs that may appear during the initial oxidation of the Pt(111) surface. For the general guidance of training-set preparation, we refer to a recent publication.[52] The reference DFT calculations are performed using VASP[47,48] with projector-augmented wave pseudopotentials.[53] We apply the Perdew−Burke−Ernzerhof functional[54] for calculating the exchange−correlation energy of electrons. The energy cutoff for the plane-wave basis set is set to 450 eV, and the spacing of **k**-points grid is smaller than 0.314 Å^{-1}. These settings satisfy convergence criteria of 10 meV/atom and 0.1 eV/Å for energy and force, respectively.

First, we sample local environments of stable and metastable Pt−O crystals, including Pt ($Fm\bar{3}m$), PtO ($P4_2/mmc$), Pt_3O_4 ($Pm\bar{3}m$), α-PtO_2 ($P6_3mc$), and β-PtO_2 ($Pnnm$), through uniaxial, hydrostatic, and shear lattice distortion within ±10% and a constant volume (NVT) MD trajectory at 600 K for 3 ps using the Nosé−Hoover thermostat.[55] The energy−distance curve of O_2 molecule is also included. Additional crystal motifs[56] and disordered configurations are sampled through melt-quench NVT MD trajectories at the Pt/O composition of 2:1. Starting with the configuration premelted at 4000 K, it is melted at 2000 K for 5 ps, and quenched to 1000 K for 10 ps. The initial and final structures for the MD simulations are shown in Figure S1. In a similar vein, the relaxation trajectories of the Pt(111) surface with randomly distributed O atoms are included to account for various local environments of the oxidized surface. In addition, the following static structures are augmented by perturbing atoms from equilibrium: a Pt(111) surface covered with various O coverage from 0 to 1 monolayer at the FCC sites,[57] a Pt(111) surface with a single adsorbed O atom at specific surface and subsurface sites,[58] and a monolayer-oxidized Pt(111) surface with α and β-PtO_2.[59] The spin-polarization is considered only for O_2 molecules, monolayer-oxidized Pt(111) surface, melt-quench MD trajectories, and relaxation

https://doi.org/10.1021/acs.jctc.4c00767
J. Chem. Theory Comput. 2024, 20, 8024−8034

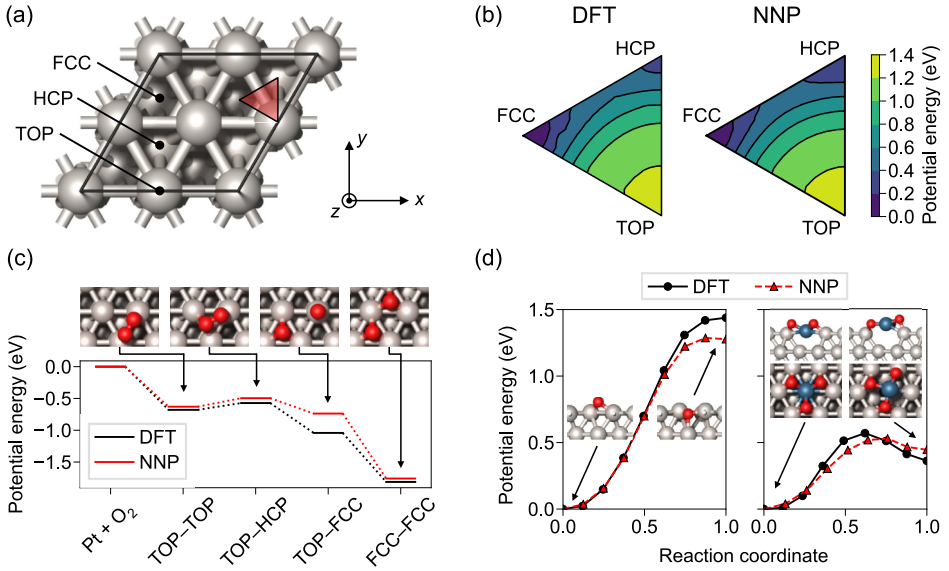

Figure 4. NNP validation on the Pt(111) surface. (a) Adsorption sites of an O atom on a 2 × 2 Pt(111) surface. The red semitransparent triangle denotes the irreducible part of the Pt(111) surface, whose PES is compared between DFT and NNP in (b). (c) Energy profiles of DFT and NNP for the dissociative adsorption path of an O_2 molecule. (d) Minimum energy paths for subsurface diffusion of the O atom from the HCP sites and the buckling reaction of the Pt atom. The silver, navy blue, and red atoms represent Pt, buckled Pt, and O atoms, respectively.

paths of Pt(111) surface with randomly distributed O atoms. In total, the data set consists of 7149 configurations with 402,515 training points (see Table S1).

The Behler–Parrinello-type NNP[40] is trained using the `SIMPLE-NN` package.[60] Atom-centered symmetry functions encode the local environments within a 6 Å radius.[61] The radial and angular parts consist of 16 and 54 features, respectively. To enhance convergence in training, the input features are decorrelated via principal component analysis and whitening.[62,63] The NNP comprises two 30-node fully connected hidden layers, yielding a 70-30-30-1 structure. We divide the total data set into training and validation sets at a 9:1 ratio. As a result of training, the NNP achieves root-mean-squared errors of 7 meV/atom for energy and 0.22 eV/Å for forces on the validation set, respectively (see Figure S2).

To further validate the trained NNP, we compare results from DFT and NNP for a series of representative configurations and reactions for O atoms on the Pt(111) surface. Figure 4a shows the 2 × 2 cell of Pt(111) surface, and three symmetric adsorption sites for oxygen (FCC, HCP, and TOP) are noted. Figure 4b illustrates the PES of an O atom over the irreducible area of the Pt(111) surface (red shade in Figure 4a), which is obtained by relaxing the *z*-position for the given *xy* position, and referencing it to that of the FCC site. For NNP, the energies at the HCP and TOP sites are 0.21 and 1.24 eV, respectively; for DFT, these are 0.32 and 1.21 eV. Notably, the NNP indicates a slightly higher stability (by 0.11 eV) at the HCP site compared to DFT, yet the overall stability order among sites is similar between NNP and DFT.

In Figure 4c, we explore the energy profile as the O_2 molecule dissociatively adsorbs onto the surface.[64] The reference energy is defined as the sum of the energies of the pristine Pt(111) surface and the isolated O_2 molecule (Pt + O_2). It is seen that the energy profile from NNP is close to that of DFT throughout the adsorption pathway, with an error within 0.1 eV, except for the TOP–FCC configuration, which shows a deviation of 0.3 eV. This discrepancy may be due to the under-sampling of the unstable TOP site configurations in the training data.

In Figure 4d, we examine the minimum energy paths for out-of-plane reactions, specifically the subsurface diffusion of an O atom at the HCP sites and the buckling reactions of the Pt atoms, using the nudged elastic band method.[13] During the buckling reaction, a surface Pt atom with sufficient adsorbed oxygen atoms is lifted from the lattice site to approximately the height of adsorbed oxygen atoms, shaping a Pt–O planar structure and generating a vacancy beneath.[37] The energies of the IS serve as a reference. These reactions are crucial for understanding the initial stages of Pt surface oxidation.[57] Due to the extensive collective motions involved, the calculations are performed on 3 × 3 surface unit cells. The NNP accurately captures the minimum energy paths of these processes with an error margin of less than 0.2 eV. Notably, our training set does not explicitly include these diffusion trajectories, underscoring the reliability of NNP as a surrogate for DFT in saddle point searches on the oxidized Pt(111) surface.

Unlike manually generated reactions from previous validations, unexpected reactions can also be identified during saddle point search using NNP. To enhance the reliability of these NNP-predicted pathways and improve the accuracy of the NNP on-the-fly, a hybrid approach where DFT is employed to verify key reaction pathways would be beneficial. To efficiently select reactions for DFT validation, techniques such as uncertainty quantification[65] or clustering-based sampling[66] could be used.

3.2. Performance Comparison of ARTn Methods.

Utilizing the NNP trained in the above, we attempt to find the saddle points connected to the model system in Figure 3 employing original, smooth-, and iso-ARTn methods. In total, 5000 runs are independently performed to identify saddle points. Each run first generates the initial active volume V_0 defined as a sphere with a radius of 6 Å, centered at a randomly selected surface atom. The randomly generated push vector $\hat{\mathbf{e}}_{\mathrm{ini}}$ is assigned to the atoms within V_0. Then, three types of ARTn methods are applied to the identical initial condition, and

https://doi.org/10.1021/acs.jctc.4c00767
J. Chem. Theory Comput. 2024, 20, 8024–8034

Table 1. Performance Comparison of the Original, Smooth-, and Iso-ARTn Methods with Adaptive Active Volume Across 5000 Saddle Point Searches[a]

	connected (%)	disconnected (%)	unconverged (%)	n^{TS} ($\tilde{n}^{TS}$)	$\langle f \rangle$
original ARTn	79.5	**11.0**	9.5	221 (80)	1647.8
smooth-ARTn	56.9	41.1	2.0	**263** (75)	1493.2
iso-ARTn	**87.7**	11.4	**0.9**	244 (**82**)	**961.9**

[a] n^{TS} and $\tilde{n}^{TS}$ denote the total number of unique saddle points and the subset with barrier energies lower than 1.3 eV, respectively. $\langle f \rangle$ represents the average number of force calls.

terminated if the number of iterations exceeds 500 or the system converges to a saddle point. The active volume is updated adaptively as described in Section 2.3 (its effect is analyzed at the end of this subsection.) The convergence criteria (ϵ) for the magnitude of the force vector at the saddle point is set to 0.01 eV/Å. The maximum step size (Δr_{max}) for the activation step is set to 0.1 Å. Below the inflection hyperplane, the orthogonal relaxation is conducted for one step. For smooth-ARTn, the mixing coefficient (η) linearly increases from 0 to 1 over three ARTn iterations as λ changes from positive to negative (see eq 3). Iso-ARTn applies the constraint on the hyperplane until λ remains negative for three consecutive ARTn iterations.

We evaluate the performance of each method based on three metrics: success rate, diversity, and computational cost. The success rate measures the probability that the method identifies relevant saddle points. For this purpose, we classify the search results into three categories: connected, disconnected, and unconverged. In a connected case, the method successfully identifies a relevant saddle point along the minimum energy path connecting the IS and FS. In a disconnected case, the method finds a saddle point unrelated to the IS, i.e., a small push along $\hat{\mathbf{e}}_{min}$ does not return to the starting harmonic basin. In an unconverged case, the method fails to identify any saddle point within 500 iterations. On the other hand, to assess diversity in identified saddle points, we count the number of unique saddle points (n^{TS}). We also enumerate those with barrier energies lower than 1.3 eV as $\tilde{n}^{TS}$, which are the main events under normal conditions. Two saddle points are considered identical if all atomic coordinates in their configurations overlap within a tolerance of 0.4 Å. We employ a relatively large tolerance because the saddle point usually has a smaller curvature than the local minimum, so even when converged under the same force tolerance, there is a larger positional deviation. Lastly, the computational cost can be well measured by the number of force calls since the force evaluations in the activation, relaxation, and Lanczos method, take most of the computational time.

Table 1 summarizes the performances of the three ARTn methods. Original ARTn achieves a connected case rate of 79.5%, with disconnected and unconverged cases at 11.0 and 9.5%, respectively. Among connected cases, only 221 saddle points are unique (n^{TS}), with 80 of them having a barrier energy lower than 1.3 eV ($\tilde{n}^{TS}$). The average number of force calls during 5000 saddle-point searches is 1647.8. Next, smooth-ARTn shows a lower success rate of 56.9%, with approximately four times more disconnected cases at 41.1%. While n^{TS} increases to 263, $\tilde{n}^{TS}$ decreases to 75. The average number of force calls is slightly reduced to 1493.2. Lastly, iso-ARTn attains the highest success rate of 87.7%, with significantly fewer unconverged cases at 0.9%. Although n^{TS} from iso-ARTn is 244, fewer than 263 from smooth-ARTn, it has the largest $\tilde{n}^{TS}$ of 82. Notably, the average number of force calls is reduced significantly compared to the original and smooth-ARTn methods.

In ref 33, a trade-off was found between the diversity of saddle points and a high success rate. This is because active movements toward various saddle points can cause the system to traverse basin boundaries, often leading to disconnected cases. This is also confirmed in Table 1 where smooth-ARTn sacrifices its success rate to identify a broader variety of saddle points (263), compared to 221 in the original ARTn. However, iso-ARTn appears to defy this trade-off by achieving a higher success rate while identifying a more diverse set of saddle points (244), compared to the original ARTn. Furthermore, when considering saddle points with barrier energies less than 1.3 eV, iso-ARTn outperforms smooth-ARTn in diversity.

To investigate the impact of the adaptive active volume, we also conduct experiments using the original ARTn with a fixed active volume, defined initially and not updated during the saddle point searches. With this fixed active volume, the success rate for connected cases drops from 79.5 to 76.6%. Concurrently, the rates for disconnected and unconverged cases increase from 11.0 and 9.5% to 13.1 and 10.3%, respectively. Additionally, the diversity of identified saddle points is adversely affected, with n^{TS} ($\tilde{n}^{TS}$) decreasing from 221(80) to 217(76). This degradation in both the success rate and diversity with a fixed active volume highlights the importance of adaptively updating active volume based on the atomic displacement during saddle point searches. For a visualization of the evolution of adaptive active volume during saddle point search, refer to Supporting Video S1.

3.3. Analysis on the Performance. To understand different success rates among the ARTn methods, we analyze an exemplary case in which original, smooth-, and iso-ARTn lead to unconverged, disconnected, and connected saddle points, respectively. In the corresponding reaction, the O atom at the HCP site moves to a nearby FCC site. In Figure 5, $|\mathbf{d}|$, the magnitude of the displacement from $\mathbf{r}_0$, is plotted as a function of the ARTn step with the activation and orthogonal relaxation steps. The degree of alignment between $\mathbf{d}$ and $\mathbf{F}_\perp^{(\prime)}$ is color-coded by $|\hat{\mathbf{d}}\cdot\hat{\mathbf{F}}_\perp^{(\prime)}|$. The gray-shaded areas mean the ARTn methods have a negative λ in the corresponding steps.

As the system departs from the IS, $|\mathbf{d}|$ of all ARTn methods increases until λ becomes negative, entering the inflection hyperplane. For the original ARTn in Figure 5a, when λ turns negative, $\mathbf{F}_\perp$ aligns antiparallel to $\mathbf{d}$ such that the system is relaxed toward the IS during orthogonal relaxation as long as $|\mathbf{F}_\perp| < |\mathbf{F}_\parallel|$. (We recall that ARTn does not update the minimum mode during relaxation due to the high computational cost of the Lanczos method.) Consequently, the original ARTn repeats this cycle, leading to an unconverged case. In contrast, smooth-ARTn in Figure 5b follows an identical trajectory to the original ARTn until λ first becomes negative. However,

https://doi.org/10.1021/acs.jctc.4c00767
J. Chem. Theory Comput. 2024, 20, 8024−8034

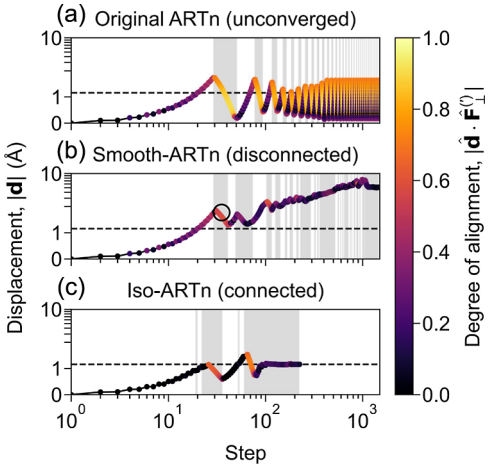

Figure 5. Displacement and degree of alignment along the saddle point search trajectories of three ARTn methods. The horizontal dashed line represents the distance from the IS to the saddle point. In gray-shaded areas, the ARTn methods have a negative λ.

above the inflection hyperplane, $|\hat{\mathbf{d}}\cdot\hat{\mathbf{F}}_\perp|$ is smaller than those of the original ARTn because $\hat{\mathbf{e}}$ smoothly changes from $\hat{\mathbf{e}}_{ini}$ to $\hat{\mathbf{e}}_{min}$ (see the circle). This prevents the system from returning to the IS directly even after $\hat{\mathbf{e}}$ fully transitions to $\hat{\mathbf{e}}_{min}$. Although the system avoids falling back into the IS, the mismatch between $\hat{\mathbf{e}}$ and $\hat{\mathbf{e}}_{min}$ in smooth-ARTn allows it to traverse the basin boundary, eventually identifying a disconnected saddle point.

Lastly, iso-ARTn Figure 5c reaches the inflection hyperplane with approximately half $\hat{\mathbf{d}}$ of the other methods because it applies the constraint to the relaxation hyperplane even when λ is positive. As the system escapes the harmonic basin, the change in $\hat{\mathbf{d}}$ is suppressed due to orthogonality between $\mathbf{d}$ and $\mathbf{F}'_\perp$ (see eq 4). After the constraint on the hyperplane is lifted after three ARTn iterations, the system successfully relaxes to locate the saddle point within 200 steps. The additional constraint in $\mathbf{F}'_\perp$ prevents the system from returning to the IS or drifting to other basins. For the whole saddle point search trajectories of three ARTn methods, refer to Supporting Video S2.

Next, we examine in detail the number of force calls between methods by dividing it according to the search results. In Figure 6a, the numbers of force calls are well separated between search results and also relatively consistent across the methods. On average, while a connected case requires only approximately 500 force calls, a disconnected case needs 2500 to be converged. An unconverged case consumes around 7500 force calls without identifying saddle points. Due to the distinct number of force calls between results, even a small change in the success rate significantly affects the average number of force calls (see Figure 6b). In the original ARTn, while unconverged cases account for only 9.5% of saddle point searches, they increase the average number of force calls by 671.3. Even though a disconnected case in smooth-ARTn constitutes a large portion of the number of force calls by 974.1, the average number of force calls is slightly decreased compared to the original ARTn due to a lower ratio of an unconverged case of 2.0%. The iso-ARTn achieves the smallest number of force calls by reducing the ratio of unconverged cases to 0.9%.

3.4. Completeness of Reactions Identified with Iso-ARTn. In the previous subsections, we demonstrated the efficiency of the iso-ARTn in terms of success rate, diversity, and computational cost. One may further question whether iso-ARTn can identify every possible reaction, a requirement for on-the-fly kMC simulations. To address this, we conduct 10,000 saddle point searches with iso-ARTn under the same conditions above and compare the resulting saddle points with a reference event table.

The barrier energies and trial numbers of the identified saddle points are presented in Figure 7. For duplicated saddle points, we only show the first instance identified. The barrier energy distribution of unique saddle points is shown on the right side of Figure 7. The bimodal distribution of barrier energies arises because only reactions involving Pt vacancy formation require high energy to break bonds. We here focus on the reactions with barrier energy below 1.3 eV (see the red dashed line in Figure 7) for a practical purpose. The reactions with barrier energy below 1.3 eV primarily involve O diffusion and buckling of Pt atoms. An O atom at the surface can migrate between neighboring FCC and HCP sites (in-plane diffusion) or it can move to a subsurface site (out-of-plane diffusion). The Pt buckling represents the reactions where a Pt atom lifts from the surface, pushing the nearby O atoms (see the right figure of Figure 4d). It is a concerted reaction that

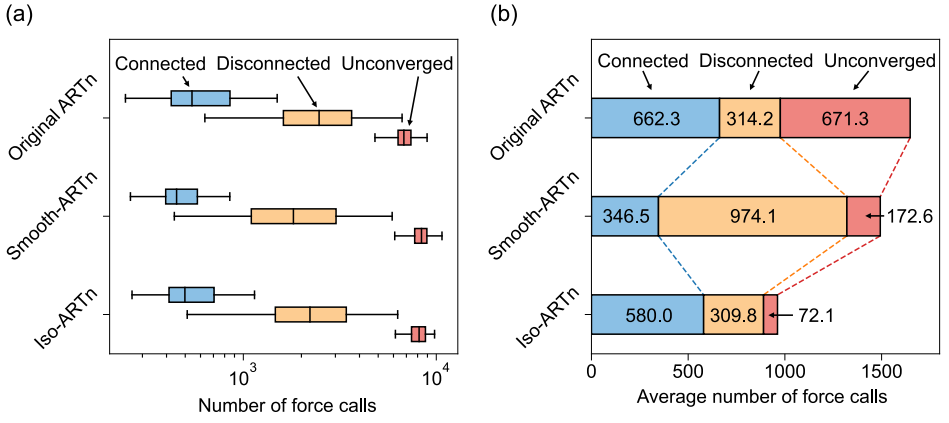

Figure 6. Analysis of the number of force calls of three ARTn methods. (a) Distribution of force calls of ARTn methods by saddle point search results. (b) Average number of force calls for three ARTn methods.

https://doi.org/10.1021/acs.jctc.4c00767
J. Chem. Theory Comput. 2024, 20, 8024−8034

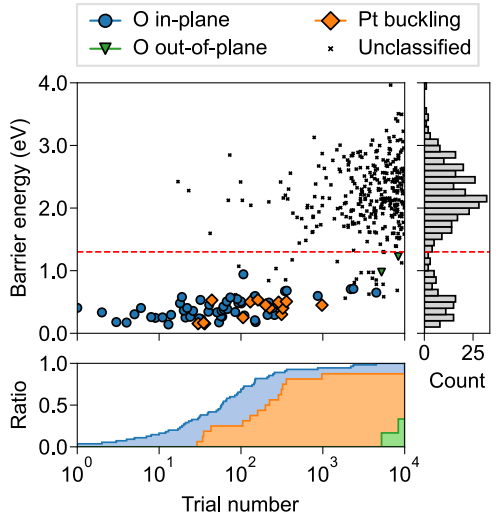

Figure 7. Barrier energy and trial number of reactions sampled during 10,000 random searches with iso-ARTn. The distribution of barrier energy is shown on the right side. The identified ratios of each reaction type are depicted on the bottom side. The red dashed line stands for a barrier energy of 1.3 eV.

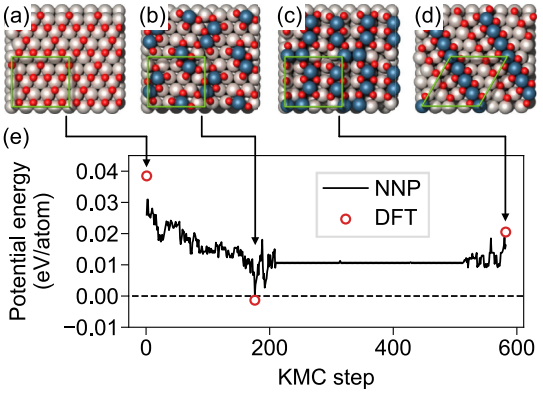

Figure 8. Results of on-the-fly off-lattice kMC simulation for Pt-oxidation with iso-ARTn. (a) The initial, (b) the lowest, and (c) the last structures are shown with 2 × 2 in-plane replication for a broader view. (d) Clustered Pt-buckled structure suggested in ref 57. The silver, navy blue, and red atoms indicate the Pt, buckled Pt, and O atoms, respectively. (e) Energy profile of the kMC simulation.

accompanies the rearrangement of Pt and O atoms simultaneously.

For a reference event table, we manually enumerate all conceivable reactions related to the O diffusion and Pt buckling. This results in 55, 6, and 16 reactions for O in-plane diffusion, O out-of-plane diffusion, and Pt buckling, respectively (see Supporting Information for details). The ratios of identified saddle points over reference saddle points for three categories are depicted as a cumulative histogram at the bottom of Figure 7. Iso-ARTn successfully identifies all O in-plane diffusion reactions in 10,000 random searches. However, it detected 2 of 6 (33%) reactions for O out-of-plane diffusion and 14 of 16 (88%) for Pt buckling. Note that although Pt buckling is a collective motion, iso-ARTn discovers most of them. The six missing reactions could be successfully identified by setting $\hat{\mathbf{e}}_{\mathrm{ini}}$ as a unit vector from the IS to FS. This implies that all reactions can be found in principle with a sufficiently large number of trials. However, we find that the present algorithm tends to produce the same saddle points repeatedly. To minimize redundant searches, future development could apply strategies such as orthogonalization[23] where all $\hat{\mathbf{e}}_{\mathrm{ini}}$ are orthogonal.

3.5. KMC Simulation with Iso-ARTn. We conduct an on-the-fly off-lattice kMC simulation for Pt-oxidation with iso-ARTn to showcase its applicability in constructing the event table adaptively (see Figure 8). The model system is a 4 × 4 Pt(111) slab covered with ordered 0.75 monolayers of O adatoms, where its high coverage is set for accelerated oxidation (see Figure 8a). The simulation adopts the Bortz–Kalos–Lebowitz algorithm[67] with a temperature of 298 K. We use a constant attempt frequency of 10^{13} Hz for all reactions. To maintain computational efficiency, event tables are constructed by performing 100 saddle point searches with iso-ARTn at each kMC step. For simplicity, the event table is not recycled.[68,69] Additionally, to mitigate the time-disparity problem,[70] where the system is trapped in low-lying basins, we neglect the reaction with a barrier energy of less than 0.05 eV. In total, 582 kMC steps are carried out and the elapsed time is 41 μs. During the kMC, the Pt(111) surface undergoes reconstruction due to oxidation from the initial structure (see Figure 8a–c). For comparison, in Figure 8e, we compute the DFT energies for three configurations in the initial, the lowest, and the last structure, after full relaxation (see empty circles). The energy profiles from both NNP and DFT calculations are referenced against the fully relaxed configuration shown in Figure 8d, known as the most stable structure at 0.75 monolayers.[57] The NNP and DFT energies are in reasonable agreement for the three snapshots.

As Pt atoms form Pt–O square planar units through the Pt buckling reaction, effectively stabilizing the repulsion between oxygen atoms, the energy decreases up to 200 kMC steps. After that, the energy fluctuates within thermal energy, while the system visits various states. During the kMC simulation, Pt–O square planar units induce the Pt buckling reaction in the vicinity, resulting in larger units. Interestingly, we identify the structure that is more stable by 15 meV/O atom than the clustered Pt-buckled structure at 0.75 monolayers (see Figure 8b). Notably, this structure is discovered without any human intervention. Despite being less ordered, more O atoms bonding with Pt–O square planar units stabilize the system. Consistently, similar structures featuring "spokes" or rows have also been observed in experiments.[71−73] The configurations identified during the kMC simulation underscore the capability of iso-ARTn to construct a reliable event table.

The off-lattice kMC simulation method combined with iso-ARTn can be extended to various surface applications, including catalytic reactions.[74] In systems with a high degree of freedom, particularly those involving polyatomic molecules, iso-ARTn might be advantageous for efficiently identifying the saddle points. Unlike traditional methods that depend on predefined reaction pathways,[75,76] our approach is reaction-agnostic, allowing for the discovery of previously unknown reaction pathways. However, the inclusion of molecules introduces low-barrier motions, such as molecular rotation, which may complicate the simulation by exacerbating time-scale disparities or resulting in redundant searches. Addressing these challenges will require the development of more sophisticated techniques, which we plan to investigate in future studies.

https://doi.org/10.1021/acs.jctc.4c00767
J. Chem. Theory Comput. 2024, 20, 8024−8034

4. CONCLUSIONS

In this work, we introduced the iso-ARTn algorithm and the adaptive active volume to address the challenges in previous saddle point search methods. The NNP was trained for an exhaustive saddle point search on Pt(111) surface with O atoms and exhibited high accuracy compared to DFT calculation. With its constraint on orthogonal relaxation, iso-ARTn achieved higher success rates with fewer force calls than previous ARTn methods. Meanwhile, the iso-ARTn finds more variety of saddle points, defying the trade-off relation between success rate and diversity. Additionally, despite its constraints, iso-ARTn identifies all possible reactions below a specific barrier energy. Furthermore, we conducted a Pt-oxidation kMC simulation using iso-ARTn to build an event table, where we observed structures consistent with experimental findings. This research paves the way for more sophisticated investigations into complex surface chemistry, significantly accelerating the identification of TSs.

■ ASSOCIATED CONTENT

Data Availability Statement

The SHERPA package is available at https://github.com/MDIL-SNU/SHERPA.

Supporting Information

The Supporting Information is available free of charge at https://pubs.acs.org/doi/10.1021/acs.jctc.4c00767.

Details of the training set for NNP, snapshots for MD simulations, energy and force correlations of the NNP and DFT, and the details for counting possible reactions (PDF)

Evolution of adaptive active volume during saddle point search (MP4)

Whole saddle point search trajectories of original, smooth-, iso-ARTn (MP4)

■ AUTHOR INFORMATION

Corresponding Author

Seungwu Han − *Department of Material Science and Engineering, Seoul National University, Seoul 08826, Korea; Korea Institute for Advanced Study, Seoul 02455, Korea;* orcid.org/0000-0003-3958-0922; Email: hansw@snu.ac.kr

Authors

Jisu Jung − *Department of Material Science and Engineering, Seoul National University, Seoul 08826, Korea;* orcid.org/0000-0003-2814-1289

Hyungmin An − *Department of Material Science and Engineering, Seoul National University, Seoul 08826, Korea;* orcid.org/0000-0003-2529-4247

Jinhee Lee − *Fuel Cell Center, Hyundai Motor Company, Yongin 16891, Korea*

Complete contact information is available at: https://pubs.acs.org/10.1021/acs.jctc.4c00767

Notes

The authors declare no competing financial interest.

■ ACKNOWLEDGMENTS

This work was supported by the R&D Collaboration Programs of Hyundai Motor Company and National R&D Program through the National Research Foundation of Korea (NRF) funded by Ministry of Science and Information and Communication Technology (ICT) (RS-2024-00407995). The computations were carried out at the Korea Institute of Science and Technology Information (KISTI) National Supercomputing Center (KSC-2023-CRE-0458) and the Center for Advanced Computations (CAC) at Korea Institute for Advanced Study (KIAS).

■ REFERENCES

(1) Somorjai, G. A.; Li, Y. *Introduction to Surface Chemistry and Catalysis*; John Wiley & Sons, 2010.

(2) Marcus, P. Surface science approach of corrosion phenomena. *Electrochim. Acta* **1998**, *43*, 109−118.

(3) Puurunen, R. L. Surface chemistry of atomic layer deposition: A case study for the trimethylaluminum/water process. *J. Appl. Phys.* **2005**, *97*, 121301.

(4) Voter, A. F.; Montalenti, F.; Germann, T. C. Extending the time scale in atomistic simulation of materials. *Annu. Rev. Mater. Res.* **2002**, *32*, 321−346.

(5) Sørensen, M. R.; Voter, A. F. Temperature-accelerated dynamics for simulation of infrequent events. *J. Chem. Phys.* **2000**, *112*, 9599−9606.

(6) Prinz, J.-H.; Wu, H.; Sarich, M.; Keller, B.; Senne, M.; Held, M.; Chodera, J. D.; Schütte, C.; Noé, F. Markov models of molecular kinetics: Generation and validation. *J. Chem. Phys.* **2011**, *134*, 174105.

(7) Rod, T. H.; Logadottir, A.; Nørskov, J. K. Ammonia synthesis at low temperatures. *J. Chem. Phys.* **2000**, *112*, 5343−5347.

(8) Lopez, N.; Nørskov, J. K. Catalytic CO oxidation by a gold nanoparticle: A density functional study. *J. Am. Chem. Soc.* **2002**, *124*, 11262−11263.

(9) Kim, Y.; Kim, J. W.; Kim, Z.; Kim, W. Y. Efficient prediction of reaction paths through molecular graph and reaction network analysis. *Chem. Sci.* **2018**, *9*, 825−835.

(10) Ismail, I.; Stuttaford-Fowler, H. B. V. A.; Ochan Ashok, C.; Robertson, C.; Habershon, S. Automatic proposal of multistep reaction mechanisms using a graph-driven search. *J. Phys. Chem. A* **2019**, *123*, 3407−3417.

(11) Türtscher, P. L.; Reiher, M. Pathfinder—Navigating and analyzing chemical reaction networks with an efficient graph-based approach. *J. Chem. Inf. Model.* **2023**, *63*, 147−160.

(12) Shang, C.; Liu, Z.-P. Stochastic surface walking method for structure prediction and pathway searching. *J. Chem. Theory Comput.* **2013**, *9*, 1838−1845.

(13) Henkelman, G.; Jónsson, H. Improved tangent estimate in the nudged elastic band method for finding minimum energy paths and saddle points. *J. Chem. Phys.* **2000**, *113*, 9978−9985.

(14) E, W.; Ren, W.; Vanden-Eijnden, E. String method for the study of rare events. *Phys. Rev. B* **2002**, *66*, 052301.

(15) Zimmerman, P. Reliable transition state searches integrated with the growing string method. *J. Chem. Theory Comput.* **2013**, *9*, 3043−3050.

(16) Duan, Z.; Henkelman, G. Atomic-scale mechanisms of electrochemical Pt dissolution. *ACS Catal.* **2021**, *11*, 14439−14447.

(17) Xu, J.; Xie, W.; Han, Y.; Hu, P. Atomistic insights into the oxidation of flat and stepped platinum surfaces using large-scale machine learning potential-based grand-canonical Monte Carlo. *ACS Catal.* **2022**, *12*, 14812−14824.

(18) Hare, S. R.; Tantillo, D. J. Post-transition state bifurcations gain momentum − current state of the field. *Pure Appl. Chem.* **2017**, *89*, 679−698.

(19) Jafari, M.; Zimmerman, P. M. Reliable and efficient reaction path and transition state finding for surface reactions with the growing string method. *J. Comput. Chem.* **2017**, *38*, 645−658.

(20) Jafari, M.; Zimmerman, P. M. Uncovering reaction sequences on surfaces through graphical methods. *Phys. Chem. Chem. Phys.* **2018**, *20*, 7721−7729.

(21) Mei, D.; Xu, L.; Henkelman, G. Dimer saddle point searches to determine the reactivity of formate on Cu(111). *J. Catal.* **2008**, *258*, 44−51.
(22) Mei, D.; Xu, L.; Henkelman, G. Potential energy surface of methanol decomposition on Cu(110). *J. Phys. Chem. C* **2009**, *113*, 4522−4537.
(23) Henkelman, G.; Jónsson, H. A dimer method for finding saddle points on high dimensional potential surfaces using only first derivatives. *J. Chem. Phys.* **1999**, *111*, 7010−7022.
(24) Restrepo, O. A.; Becquart, C. S.; El-Mellouhi, F.; Bouhali, O.; Mousseau, N. Diffusion mechanisms of C in 100, 110 and 111 Fe surfaces studied using kinetic activation-relaxation technique. *Acta Mater.* **2017**, *136*, 303−314.
(25) De Lile, J. R.; Mousseau, N. Diffusion of oxygen vacancies formed at the anatase (101) surface: An activation-relaxation technique study. *Phys. Rev. Mater.* **2023**, *7*, 034602.
(26) Cerjan, C. J.; Miller, W. H. On finding transition states. *J. Chem. Phys.* **1981**, *75*, 2800−2806.
(27) Banerjee, A.; Adams, N.; Simons, J.; Shepard, R. Search for stationary points on surfaces. *J. Phys. Chem.* **1985**, *89*, 52−57.
(28) Doye, J. P. K.; Wales, D. J. Surveying a potential energy surface by eigenvector-following. *Z. Phys. D: At., Mol. Clusters* **1997**, *40*, 194−197.
(29) Ohno, K.; Maeda, S. A scaled hypersphere search method for the topography of reaction pathways on the potential energy surface. *Chem. Phys. Lett.* **2004**, *384*, 277−282.
(30) Barkema, G. T.; Mousseau, N. Event-based relaxation of continuous disordered systems. *Phys. Rev. Lett.* **1996**, *77*, 4358−4361.
(31) Malek, R.; Mousseau, N. Dynamics of Lennard-Jones clusters: A characterization of the activation-relaxation technique. *Phys. Rev. E* **2000**, *62*, 7723−7728.
(32) Jay, A.; Huet, C.; Salles, N.; Gunde, M.; Martin-Samos, L.; Richard, N.; Landa, G.; Goiffon, V.; De Gironcoli, S.; Hémeryck, A.; Mousseau, N. Finding reaction pathways and transition states: r-ARTn and d-ARTn as an efficient and versatile alternative to string approaches. *J. Chem. Theory Comput.* **2020**, *16*, 6726−6734.
(33) Olsen, R. A.; Kroes, G. J.; Henkelman, G.; Arnaldsson, A.; Jónsson, H. Comparison of methods for finding saddle points without knowledge of the final states. *J. Chem. Phys.* **2004**, *121*, 9776−9792.
(34) Lanczos, C. An iteration method for the solution of the eigenvalue problem of linear differential and integral operators. *J. Res. Natl. Bur. Stand.* **1950**, *45*, 255.
(35) Henkelman, G.; Jónsson, H. Long time scale kinetic Monte Carlo simulations without lattice approximation and predefined event table. *J. Chem. Phys.* **2001**, *115*, 9657−9666.
(36) El-Mellouhi, F.; Mousseau, N.; Lewis, L. J. Kinetic activation-relaxation technique: An off-lattice self-learning kinetic Monte Carlo algorithm. *Phys. Rev. B* **2008**, *78*, 153202.
(37) Fantauzzi, D.; Mueller, J. E.; Sabo, L.; van Duin, A. C. T.; Jacob, T. Surface buckling and subsurface oxygen: Atomistic insights into the surface oxidation of Pt(111). *ChemPhysChem* **2015**, *16*, 2797−2802.
(38) Topalov, A. A.; Cherevko, S.; Zeradjanin, A. R.; Meier, J. C.; Katsounaros, I.; Mayrhofer, K. J. J. Towards a comprehensive understanding of platinum dissolution in acidic media. *Chem. Sci.* **2014**, *5*, 631−638.
(39) Miller, D.; Sanchez Casalongue, H.; Bluhm, H.; Ogasawara, H.; Nilsson, A.; Kaya, S. Different reactivity of the various platinum oxides and chemisorbed oxygen in CO oxidation on Pt(111). *J. Am. Chem. Soc.* **2014**, *136*, 6340−6347.
(40) Behler, J.; Parrinello, M. Generalized neural-network representation of high-dimensional potential-energy surfaces. *Phys. Rev. Lett.* **2007**, *98*, 146401.
(41) Cancès, E.; Legoll, F.; Marinica, M.-C.; Minoukadeh, K.; Willaime, F. Some improvements of the activation-relaxation technique method for finding transition pathways on potential energy surfaces. *J. Chem. Phys.* **2009**, *130*, 114711.
(42) Polak, E. *Computational Methods in Optimization: A Unified Approach*; Academic Press, 1971.
(43) Sheppard, D.; Terrell, R.; Henkelman, G. Optimization methods for finding minimum energy paths. *J. Chem. Phys.* **2008**, *128*, 134106.
(44) Xu, H.; Osetsky, Y. N.; Stoller, R. E. Simulating complex atomistic processes: On-the-fly kinetic Monte Carlo scheme with selective active volumes. *Phys. Rev. B* **2011**, *84*, 132103.
(45) Liang, T.; Xu, H. Saddle point search with dynamic active volume. *Comput. Mater. Sci.* **2023**, *228*, 112354.
(46) Xiao, P.; Wu, Q.; Henkelman, G. Basin constrained κ-dimer method for saddle point finding. *J. Chem. Phys.* **2014**, *141*, 164111.
(47) Kresse, G.; Hafner, J. *Ab initio* molecular dynamics for liquid metals. *Phys. Rev. B* **1993**, *47*, 558−561.
(48) Kresse, G.; Furthmüller, J. Efficient iterative schemes for *ab initio* total-energy calculations using a plane-wave basis set. *Phys. Rev. B* **1996**, *54*, 11169−11186.
(49) Thompson, A. P.; Aktulga, H. M.; Berger, R.; Bolintineanu, D. S.; Brown, W. M.; Crozier, P. S.; in 't Veld, P. J.; Kohlmeyer, A.; Moore, S. G.; Nguyen, T. D.; Shan, R.; Stevens, M. J.; Tranchida, J.; Trott, C.; Plimpton, S. J. LAMMPS − a flexible simulation tool for particle-based materials modeling at the atomic, meso, and continuum scales. *Comput. Phys. Commun.* **2022**, *271*, 108171.
(50) Larsen, A. H.; Mortensen, J. J.; Blomqvist, J.; Castelli, I. E.; Christensen, R.; Dułak, M.; Friis, J.; Groves, M. N.; Hammer, B.; Hargus, C.; Hermes, E. D.; Jennings, P. C.; Jensen, P. B.; Kermode, J.; Kitchin, J. R.; Kolsbjerg, E. L.; Kubal, J.; Kaasbjerg, K.; Lysgaard, S.; Maronsson, J. B.; Maxson, T.; Olsen, T.; Pastewka, L.; Peterson, A.; Rostgaard, C.; Schiøtz, J.; Schütt, O.; Strange, M.; Thygesen, K. S.; Vegge, T.; Vilhelmsen, L.; Walter, M.; Zeng, Z.; Jacobsen, K. W. The atomic simulation environment—a Python library for working with atoms. *J. Phys.: Condens. Matter* **2017**, *29*, 273002.
(51) Jerkiewicz, G.; Vatankhah, G.; Lessard, J.; Soriaga, M.; Park, Y. Surface-oxide growth at platinum electrodes in aqueous H_2SO_4: Reexamination of its mechanism through combined cyclic-voltammetry, electrochemical quartz-crystal nanobalance, and Auger electron spectroscopy measurements. *Electrochim. Acta* **2004**, *49*, 1451−1459.
(52) Hong, C.; Kim, J.; Kim, J.; Jung, J.; Ju, S.; Choi, J. M.; Han, S. Applications and training sets of machine learning potentials. *Sci. Technol. Adv. Mater.: Methods* **2023**, *3*, 2269948.
(53) Blöchl, P. E. Projector augmented-wave method. *Phys. Rev. B* **1994**, *50*, 17953−17979.
(54) Perdew, J. P.; Burke, K.; Ernzerhof, M. Generalized gradient approximation made simple. *Phys. Rev. Lett.* **1996**, *77*, 3865−3868.
(55) Evans, D. J.; Holian, B. L. The Nose−Hoover thermostat. *J. Chem. Phys.* **1985**, *83*, 4069−4074.
(56) Hong, C.; Choi, J. M.; Jeong, W.; Kang, S.; Ju, S.; Lee, K.; Jung, J.; Youn, Y.; Han, S. Training machine-learning potentials for crystal structure prediction using disordered structures. *Phys. Rev. B* **2020**, *102*, 224104.
(57) Hawkins, J. M.; Weaver, J. F.; Asthagiri, A. Density functional theory study of the initial oxidation of the Pt(111) surface. *Phys. Rev. B* **2009**, *79*, 125434.
(58) Gu, Z.; Balbuena, P. B. Absorption of atomic oxygen into subsurfaces of Pt(100) and Pt(111): Density functional theory study. *J. Phys. Chem. C* **2007**, *111*, 9877−9883.
(59) Shimazaki, T.; Suzuki, T.; Kubo, M. Density functional theory study on quasi-three-dimensional oxidized platinum surface: Phase transition between α-PtO_2-like and β-PtO_2-like structures. *Theor. Chem. Acc.* **2011**, *130*, 1031−1038.
(60) Lee, K.; Yoo, D.; Jeong, W.; Han, S. SIMPLE-NN: An efficient package for training and executing neural-network interatomic potentials. *Comput. Phys. Commun.* **2019**, *242*, 95−103.
(61) Behler, J. Atom-centered symmetry functions for constructing high-dimensional neural network potentials. *J. Chem. Phys.* **2011**, *134*, 074106.
(62) Wold, S.; Esbensen, K.; Geladi, P. Principal component analysis. *Chemom. Intell. Lab. Syst.* **1987**, *2*, 37−52.
(63) Yoo, D. Metadynamics Sampling for Training Machine Learning Potential. Ph.D. Thesis; Seoul National University: Seoul, 2020.

https://doi.org/10.1021/acs.jctc.4c00767
J. Chem. Theory Comput. 2024, 20, 8024−8034

(64) Yang, Z.; Wang, J.; Yu, X. Density functional theory studies on the adsorption, diffusion and dissociation of O_2 on Pt(111). *Phys. Lett. A* **2010**, *374*, 4713−4717.
(65) Jeong, W.; Yoo, D.; Lee, K.; Jung, J.; Han, S. Efficient atomic-resolution uncertainty estimation for neural network potentials using a replica ensemble. *J. Phys. Chem. Lett.* **2020**, *11*, 6090−6096.
(66) Qi, J.; Ko, T. W.; Wood, B. C.; Pham, T. A.; Ong, S. P. Robust training of machine learning interatomic potentials with dimensionality reduction and stratified sampling. *npj Comput. Mater.* **2024**, *10*, 43.
(67) Bortz, A. B.; Kalos, M. H.; Lebowitz, J. L. A new algorithm for Monte Carlo simulation of Ising spin systems. *J. Comput. Phys.* **1975**, *17*, 10−18.
(68) Xu, L.; Henkelman, G. Adaptive kinetic Monte Carlo for first-principles accelerated dynamics. *J. Chem. Phys.* **2008**, *129*, 114104.
(69) Williams, C. J.; Galindo-Nava, E. I. Accelerating off-lattice kinetic Monte Carlo simulations to predict hydrogen vacancy-cluster interactions in α-Fe. *Acta Mater.* **2023**, *242*, 118452.
(70) Andersen, M.; Panosetti, C.; Reuter, K. A practical guide to surface kinetic Monte Carlo simulations. *Front. Chem.* **2019**, *7*, 202.
(71) van Spronsen, M. A.; Frenken, J. W. M.; Groot, I. M. N. Observing the oxidation of platinum. *Nat. Commun.* **2017**, *8*, 429.
(72) Drnec, J.; Ruge, M.; Reikowski, F.; Rahn, B.; Carlà, F.; Felici, R.; Stettner, J.; Magnussen, O. M.; Harrington, D. A. Initial stages of Pt(111) electrooxidation: Dynamic and structural studies by surface X-ray diffraction. *Electrochim. Acta* **2017**, *224*, 220−227.
(73) Valls Mascaró, F.; McCrum, I. T.; Koper, M. T. M.; Rost, M. J. Nucleation and growth of dendritic islands during platinum oxidation-reduction cycling. *J. Electrochem. Soc.* **2022**, *169*, 112506.
(74) Stamatakis, M.; Vlachos, D. G. Unraveling the complexity of catalytic reactions via kinetic Monte Carlo simulation: Current status and frontiers. *ACS Catal.* **2012**, *2*, 2648−2663.
(75) Mei, D.; Rousseau, R.; Kathmann, S. M.; Glezakou, V.-A.; Engelhard, M. H.; Jiang, W.; Wang, C.; Gerber, M. A.; White, J. F.; Stevens, D. J. Ethanol synthesis from syngas over Rh-based/SiO_2 catalysts: A combined experimental and theoretical modeling study. *J. Catal.* **2010**, *271*, 325−342.
(76) Aleksandrov, H. A.; Moskaleva, L. V.; Zhao, Z.-J.; Basaran, D.; Chen, Z.-X.; Mei, D.; Rösch, N. Ethylene conversion to ethylidyne on Pd(111) and Pt(111): A first-principles-based kinetic Monte Carlo study. *J. Catal.* **2012**, *285*, 187−195.

https://doi.org/10.1021/acs.jctc.4c00767
J. Chem. Theory Comput. 2024, 20, 8024−8034